Solar Phys (2013) 284:559–578
DOI 10.1007/s11207-012-0141-3

ADVANCES IN EUROPEAN SOLAR PHYSICS

Spatially Resolved Microwave Observations of Multiple Periodicities in a Flaring Loop

E.G. Kupriyanova · V.F. Melnikov · K. Shibasaki

Received: 20 December 2011 / Accepted: 15 September 2012 / Published online: 16 October 2012

Abstract Quasi-periodic pulsations (QPPs) with at least three simultaneously existing spectral components with periods $P \geq 30$ s, $P \approx 20$ s, and about $P \approx 10$ s were detected during the decay phase of a solar flare on 3 July 2002, observed with the *Nobeyama Radioheliograph* (NoRH). A detailed study of the spatial structure of the Fourier amplitudes of QPPs along a flaring loop has revealed different spatial distributions of the three components. It is shown that the source of the QPPs with period $P \geq 30$ s has its maximum amplitude in the inner region of the loop, between the footpoints. QPPs with period $P \approx 20$ s are localized at the periphery of the loop, mainly in the outer parts of the footpoints. The spatial distribution of oscillations with period about $P \approx 10$ s contains three regions of high QPP amplitudes: two near the footpoints and one in the middle of the flaring region. It is shown that the observed properties of the spectral components are most accurately described by the fundamental, second, and third harmonics of the kink mode standing waves. This is the first identification of the kink mode in flare loops which is based on strict limitations derived from data on the spatial structure of a pulsating flare region.

Keywords Flares, impulsive phase · Oscillations, solar · Radio bursts, microwave

Advances in European Solar Physics
Guest Editors: Valery M. Nakariakov, Manolis K. Georgoulis, and Stefaan Poedts

E.G. Kupriyanova (✉) · V.F. Melnikov
Central Astronomical Observatory at Pulkovo of the Russian Academy of Sciences,
Saint-Petersburg 196140, Russia
e-mail: elenku@bk.ru

V.F. Melnikov
Purple Mountain Observatory, Nanjing, China

K. Shibasaki
Nobeyama Solar Radio Observatory, Minamimaki, Minamisaku, Nagano 384-1305, Japan

1. Introduction

Quasi-periodic pulsations (QPPs) of flare radio emission with periods from several seconds to several minutes are a good tool for flare plasma diagnostics due to their close connection with magnetohydrodynamic (MHD) waves in coronal loops (for a review see Nakariakov and Melnikov, 2009; Nakariakov and Verwichte, 2005). The presence of QPPs in light curves is quite a common, if not intrinsic, phenomenon of flare radio emission from single flaring loops (Kupriyanova *et al.*, 2010). Moreover, some studies reported on multiple periodicities in flaring light curves, with periods ranging from several seconds to several minutes. Using spatially unresolved data from the *Nobeyama Radioheliograph* (NoRH), Stepanov *et al.* (2004) found QPPs with periods of 14 s, 7 s, and 2.4 s simultaneously present in the microwave emission time profile of the 28 August 1999 flare. The QPPs with $P \approx 14$ s and $P \approx 7$ s were explained as a radio response to the fundamental and second harmonics of the flute (ballooning) mode. Mészárosová *et al.* (2006) and Stepanov *et al.* (2009) showed the presence of multiple periodicities in integrated radio and X-ray emission of solar flares with long periods: from 1 to 10 min.

The ratio of periods of the simultaneously existing spectral components is important for determining the nature of the pulsations. Different periods of QPPs may be associated either with different MHD modes simultaneously present in a flaring loop or with different harmonics of the same MHD mode (Andries, Arregui, and Goossens, 2005; Inglis and Nakariakov, 2009). However, the identification of specific oscillatory modes is very ambiguous in the case of data analysis without spatial resolution. Analysis of the spatial distribution of QPP characteristics using data with high spatial resolution can increase the certainty of the identification. Nakariakov, Melnikov, and Reznikova (2003) and Melnikov *et al.* (2005) studied the amplitude and phase distribution along a single flaring loop for QPPs with periods of 8 – 11 s and 14 – 17 s using NoRH and *Yohkoh Hard X-Ray Telescope* (HXT) data from the flare of 12 January 2000. As a result, for the first time the global sausage mode of MHD oscillations in a flaring loop was identified, and ample evidence of the simultaneous presence of the fundamental and second harmonics of the sausage mode was obtained. This knowledge allowed the researchers to get strong limitations on the magnetic field, plasma density, and temperature in the flaring loop.

In this paper we study in detail the spatial structure of the microwave pulsations of a particular flaring loop using advanced spectral and image analysis techniques. For this study, we have chosen the flare on 3 July 2002, which is ideal for our task. It was detected by NoRH with high angular (5″ at 34 GHz and 10″ at 17 GHz) and temporal (up to 100 ms) resolution and showed interesting, and rather contradictory properties of its QPPs. Kupriyanova *et al.* (2010) used the spatially unresolved signal of this flare (NoRH correlation amplitudes) and found simultaneously existing Fourier components with periods $P \approx 20$ s and $P \approx 30$ s. At the same time, their wavelet analysis showed the presence of only one spectral component, but with the drift of its period from $P \approx 20$ s up to $P \approx 30$ s.

The paper is organized as follows. Section 3 describes the results of the spatially unresolved analysis of microwave emission from the observed flaring loop. Section 4 is devoted to a study of the spatial structure of QPPs. In Section 5 we discuss appropriate characteristics of MHD modes for the spatial, temporal, and spectral characteristics of the observed QPPs. In Section 6 the main findings of the study are summarized.

2. Method of QPP Analysis

To analyze the oscillatory structure of time profiles of any physical parameter $f_i = f(t_i)$ (original signal), we have used the method described in the paper of Kupriyanova *et al.*

(2010). First, time profiles of the low-frequency component $f^{\rm sm}(t_i)$ are found by smoothing the original signal time profiles $f(t_i)$ with an interval τ using a running average method. After smoothing, the high-frequency component is picked out by subtracting the low-frequency component from the original signal:

$$f_\tau^{\rm hf}(t_i) = f(t_i) - f_\tau^{\rm sm}(t_i). \tag{1}$$

Then, the modulation depth is calculated:

$$\Delta_\tau(t_i) = f_\tau^{\rm hf}(t_i)/f_\tau^{\rm sm}(t_i). \tag{2}$$

A presence of QPPs in the resulting time profile and their periods are checked by methods of autocorrelation, Fourier, and wavelet (Morlet) analyses. In order to avoid the appearance of false periodicities due to filtering, we repeat the procedure for a broad range of smoothing intervals τ from 5 to 50 s. A spectral component that really belongs to the signal is clearly seen in a Fourier spectrum and keeps its period for all τ. This technique was tested over a set of different model functions with a large number of trials, and showed a good degree of reliability (Kupriyanova *et al.*, 2010).

3. Spectral Properties of Spatially Unresolved QPPs

The integrated (spatially unresolved) signal used for the spectral analysis by Kupriyanova *et al.* (2010) is calculated by averaging the amplitudes of the observed correlation coefficients between signals received by pairs of remote independent single antennas of NoRH. The mean correlation amplitude represents an integrated radio flux measured from fine spatial structures (compact flaring sources) smaller than about 24″. The advantages of these observations for QPP studies are their very high sensitivity, freedom from possible instrumental phase effects (like jitter), and efficient elimination of background emission from the Sun, the Earth's atmosphere, and other objects.

In Figure 1 we show the main temporal and spectral properties of the spatially unresolved signal of the flare on 3 July 2002 observed by NoRH in the period 02:09:12 – 02:17:12 UT. The normalized time profile of correlation amplitudes ($F_{\rm ca}(t_i)$) is shown in Figure 1a by the thick black curve. The time profile displays two strong impulsive peaks and a weak smooth peak in the final phase of the burst. The modulation depth signal ($\Delta_{{\rm ca}\tau}(t_i)$) is obtained from this time profile using Equation (2) and is used for the following spectral analysis. As already mentioned, Kupriyanova *et al.* (2010) noticed an interesting drifting feature on the wavelet spectrum of QPPs during the final phase of this flare. This feature is shown in colors in Figure 1a in the time interval from the vertical dashed line to the end of the event. In Figure 1b, this part of the wavelet spectrum (from 02:13:30 to 02:17:30 UT) is presented on an enlarged scale. On the periodograms of the autocorrelation functions of $\Delta_{{\rm ca}\tau}(t_i)$ (Figure 1c) there are two well pronounced spectral peaks with periods corresponding to the lower and upper limits of the frequency drift, $P \approx 22$ s and $P \approx 30$ s. The position of each spectral peak does not depend on the value of the smoothing interval τ. This indicates that the spectral components are real, and not artifacts of filtering. On the periodograms, one can also see a set of weak spectral components with periods around $P \approx 14$ s. The independence of the secondary peaks with periods 22 s and 14 s has been checked by applying the Fourier spectral filter to the original signal. We filtered out the strong spectral peak with period 30 s using the Fourier filter with flat top (from 8 s to 25 s) and Gaussian wings. The periodogram of the filtered time series is overplotted by a black curve in Figure 1c. One can see that the spectral power of peaks around $P = 14$ s is decreased. Hence, these 14 s peaks probably are

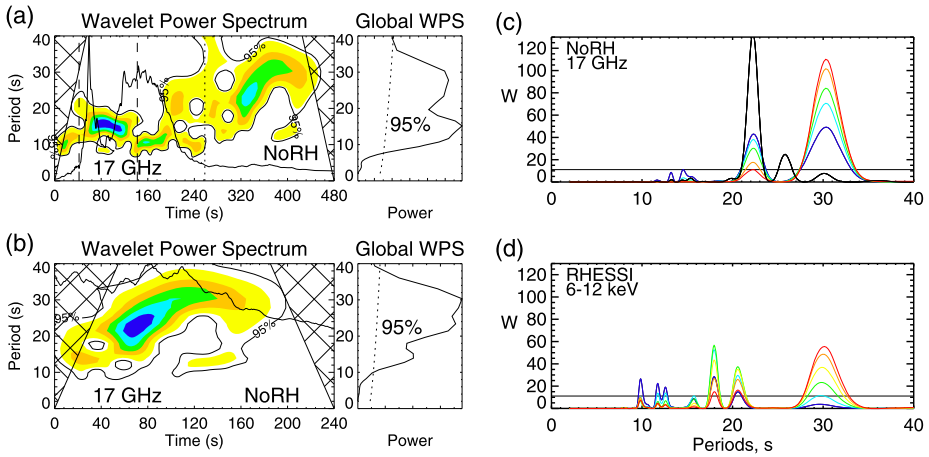

Figure 1 Temporal and spectral properties of the spatially integrated signal of the flare on 3 July 2002 02:09:12 – 02:17:12 UT detected with NoRH at 17 GHz. (a) The wavelet power spectrum (WPS) of $\Delta_{\mathrm{car}\tau}(t_i)$ for $\tau = 15$ s. The superimposed normalized time profile of the total signal is shown by a thick black line. The time interval from the vertical dotted line to the end of the event indicates the occurrence of the QPP with drifting period. The small panel to the right of the WPS is the global WPS. The dashed line shows the 95 % significance level. (b) Zoomed wavelet spectrum of the QPPs with drifting period, from 02:13:30 to 02:17:30 UT. (c) Periodograms of the autocorrelation functions of $\Delta_{\mathrm{car}\tau}(t_i)$ for the set of smoothing intervals τ; blue, pale blue, green, orange, and red solid lines correspond to $\tau = 15$, 20, 25, 30, and 35 s, respectively. The x axis represents the period in seconds, and the y axis the spectral power. The black curve is the periodogram of the filtered signal. (d) Periodograms of the RHESSI X-ray intensity modulation depth for the set of smoothing intervals τ; blue, pale blue, green, yellow, orange, and red solid lines correspond to $\tau = 16$, 20, 24, 28, 32, and 36 s, respectively. The horizontal lines on panels (c, d) indicate 99 % significance level $W_{\mathrm{sign}} \approx 11.4$.

Table 1 List of the periods.

No.	Notation	Limits, [s]	$\langle P\rangle \pm \Delta P$, [s] (NoRH, boxes)	$\langle P\rangle \pm \Delta P$, [s] (NoRH, corr. ampl)	$\langle P\rangle \pm \Delta P$, [s] (RHESSI, 6 – 12 keV)
1	$\langle P\rangle_1^{\mathrm{I}}$	[33.0, 40.0]	34.9 ± 3.0	–	–
2	$\langle P\rangle_2^{\mathrm{I}}$	[28.0, 33.0]	31.2 ± 2.5	30.1 ± 2.5	29.9 ± 2.5
3	$\langle P\rangle_1^{\mathrm{II}}$	[20.5, 22.5]	21.3 ± 1.5	22.2 ± 1.5	20.6 ± 1.5
4	$\langle P\rangle_2^{\mathrm{II}}$	[18.2, 19.8]	18.7 ± 1.0	–	18.0 ± 1.0
5	$\langle P\rangle_3$	[15.7, 17.9]	16.4 ± 0.7	–	*15.7 ± 0.7*
6	$\langle P\rangle_4$	[13.0, 14.0]	13.3 ± 0.5	–	13.3 ± 0.5
7	$\langle P\rangle_5$	[12.0, 13.0]	12.3 ± 0.4	–	12.5 ± 0.4
8	$\langle P\rangle_1^{\mathrm{III}}$	[11.3, 11.6]	11.5 ± 0.4	–	11.8 ± 0.4
9	$\langle P\rangle_2^{\mathrm{III}}$	[9.6, 10.5]	9.8 ± 0.3	–	9.8 ± 0.3

false periodicities due to side lobes of the 30 s spectral component. In contrast, the spectral power of the peak with period 22 s is strongly increased. This confirms its independence from the 30 s peak. The periods of these two spectral components are listed in the fifth column of Table 1.

To be sure that the periods found from microwave data have solar origin, we carried out a spectral analysis of the intensity variations of the hard X-ray (HXR) emission obtained with the *Reuven Ramaty High Energy Solar Spectroscopic Imager* (RHESSI). Due to the rather low HXR intensity $I_{\mathrm{HXR}}(t_i)$ of the flare during its decay phase we limited our analysis, studying only the spatially unresolved signal which is obtained by integration of the intensity over the whole flaring area. RHESSI data have temporal resolution $\Delta t = 4$ s. In order to adequately compare the spectrum of X-ray data with the spectrum of radio data obtained with resolution $\Delta t = 1$ s, we determined the function $I_{\mathrm{HXR}}(t_i)$ on the grid with cadence $\Delta t = 1$ s using a spline interpolation. Then we applied the same procedure of spectral analysis, as for microwave data, to all RHESSI energy channels. Panel (d) in Figure 1 shows periodograms of $\Delta_{\tau \mathrm{HXR}}(t_i)$ for 6 – 12 keV channel for the set of $\tau = 16$, 20, 24, 28, 32, 36 s marked by different colors. One can see that the spectral components in the periodograms are split into three groups with periods close to 30 s, 20 s, and 10 s. The obtained periodicities are similar to those found for the microwave emission although obtained using a completely independent instrument. We believe this is a strong evidence of the solar origin of the periodicities.

It is interesting that a similar combination of periods was found by Inglis and Nakariakov (2009), who studied in detail QPPs of the integrated microwave and HXR emission during the second impulsive peak of this flare. They found three spectral components of QPPs with periods 28 s, 18 s, and 12 s existing simultaneously. These spectral components were explained as being related to the kink mode. Our current extensive analysis of the flare with high spatial resolution shows that the geometry of the flare region is very similar during the whole flare, from its impulsive phase until the smooth final phase. Probably this similar combination of periods is just a consequence of the same types of MHD oscillations in the same flaring loop.

4. Analysis of the QPP Spatial Structures

4.1. Geometrical Characteristics of the Flaring Loop

The flare on 3 July 2002 was the only energetic event on the solar disk. Its coordinates were $S19W48$. In order to explore the spatial structure of QPPs in the final phase of this flare, radio maps of the flare have been built using NoRH data at 17 GHz at each moment of time t_i ($i = 1, \ldots, N-1$, where $N = 211$) from 02:13:40 to 02:17:10 UT with a time step of 1 s. An example of the radio maps is presented in Figure 2a. The radio map shows two distinct radio sources, northern and southern. Figure 2c shows that, at the beginning, the southern source (thick line) was brighter than the northern one (thin line). However, by the middle of the time interval, the northern source became brighter. The radio flux from the northern source achieved its maximum at time $t_{73} = 02{:}14{:}53$ UT, simultaneously with the maximum of the spatially unresolved signal (the correlation amplitude).

We associate these two sources with regions close to the two conjugate footpoints of a single flaring loop. In order to estimate the length of the loop at each time t_i, the distance $d_i = d(t_i)$ between the centers of the northern and southern radio brightness sources was calculated. The average over time value of the distance equals $d \approx 13$ pixels. Under the assumption of a semicircular loop, its length is $L = \pi d/2 \approx 20$ pixels. Note that the position of sources relative to each other is rather stable. The distance between them varies only within 1.5 pixels.

To estimate the radius of the cross section of the loop, the cross sections through radio brightness centers of the northern and southern radio sources at each moment of time t_i are

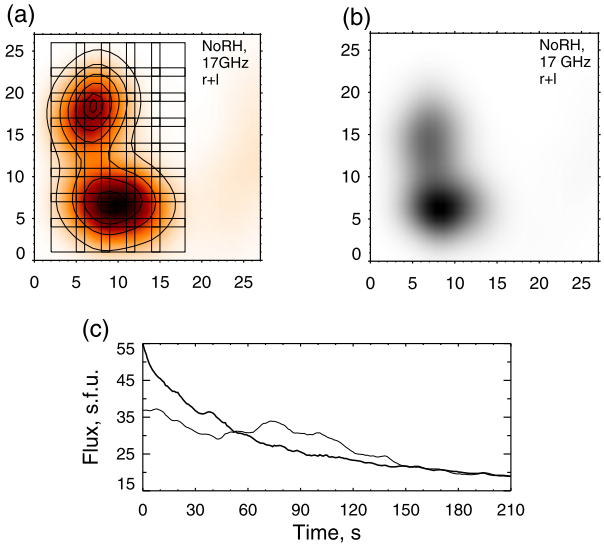

Figure 2 (a) Distribution of the radio brightness according to NoRH data at 17 GHz at time $t_0 = 02{:}13{:}40$ UT corresponding to the beginning of the final phase of the flare. The distribution of the radio brightness is shown with different degrees of shading. The horizontal and vertical axes represent the number of pixels, 1 pixel = 2.45″. Contours show the levels 0.1, 0.3, 0.5, 0.7, 0.9, and 0.97 of $F^{\max}$. $F^{\max}$ is the maximal intensity over the entire image at time $t_{73} = 02{:}14{:}53$ UT corresponding to the maximum of the integral (spatially unresolved) radio flux in the final phase of the flare. Two radio sources, northern (upper) and southern (bottom), are well pronounced. (b) The variance map obtained using Equation (3). (c) Radio flux temporal variations (in SFU) from the southern source (thick line) and northern source (thin line). The fluxes are calculated for the time interval from 02:13:40 to 02:17:10 UT from the boxes of size $20'' \times 20''$ located in the centers of the sources.

calculated and their semi-widths $a_i^{1,2}$ are determined. Here the superscripts 1 and 2 denote the northern and southern sources, respectively. The radius of the loop cross section is set as $a = \frac{1}{N}\sum_{i=0}^{N-1}(a_i^1 + a_i^2)/2$ and is equal to $a \approx 4$ pixels. Taking into account that 1 pixel $\approx 2.5''$ for our images, we obtain the absolute values of $a \approx 6600$ km and $L \approx 35\,000$ km. Note that the loop radius is comparable to the NoRH beam size, and we can consider the estimate only as its upper limit. From this, we can find an important characteristic of the flaring loop, the radius-to-length ratio, $a/L \leq 1/5$.

4.2. Method of QPP Spatial Structure Analysis

We performed our spatially resolved analysis of QPPs in the local coordinate system of the flaring loop. For this, as well as to reduce the probability of detecting some instrumental effects, like a jitter, we have stabilized the whole radio image relative to the center of brightness of the northern source. Figure 2b shows the variance map of the stabilized data cube of radio fluxes. The variance map was computed as the difference between the mean squared value of the data cube and the square of its mean value,

$$\sigma_{jk} = \sqrt{\sum_{i=0}^{N-1} F^2/N - \left(\sum_{i=0}^{N-1} F\right)^2 \Big/ N^2}. \tag{3}$$

Here $F \equiv F_{jki}$ is a pixel-by-pixel three-dimensional array of total radio fluxes after the stabilization, and j, k, i are the subscripts through the x, y, and time axes. The brightness

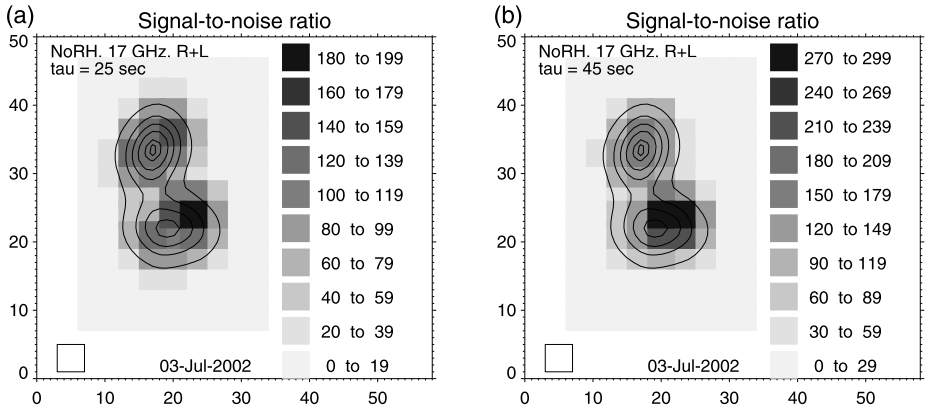

Figure 3 Maps of the signal-to-noise ratio of pulsations in the flaring region for $\tau = 25$ s (a) and for $\tau = 45$ s (b). The horizontal and vertical axes represent the number of pixels, 1 pixel $\approx 2.5''$. The discrete scale from dark to light refers to the decrease of signal-to-noise ratio from maximal to minimal value. Contours show the levels 0.1, 0.3, 0.5, 0.7, 0.9, and 0.97 of $F^{\max}$. Here $F^{\max}$ is the maximal flux over the image at time $t_{73} = 02{:}14{:}53$ UT. The box in the bottom left corner is taken as a reference for the calculation of the noise level.

distribution in the variance map indicates that there were no jumps in the position of the flaring area as a whole due to a possible instrumental (jitter) effect. Otherwise, we would see a darker ring around the flaring area. Instead, one can see that all brightness changes occur in the two radio source regions, especially in the southern one, and between them.

To explore the spatial structure of the QPPs, the flaring region is divided into 40 boxes (Figure 2a). For a quasi-continuous analysis of the spatial structure, the adjacent rows and columns of the boxes are overlapped by 1 pixel. The overlapping areas are seen as the narrow vertical and horizontal stripes in Figure 2a. The size of each box is selected to be equal to 4×4 pixels $\approx 10'' \times 10''$ in order to provide the necessary signal-to-noise ratio. This size is comparable to the NoRH beam size at 17 GHz. For each box, data are processed in an identical fashion. First, we find time profiles of the emission flux density $F(t_i)$ (Stokes I) from each box. Then we determine the high-frequency component $F_\tau^{\mathrm{hf}}(t_i)$ and the modulation depth $\Delta_\tau(t_i)$ using Equations (1) – (2).

In order to determine the area where pulsations are significant, signal-to-noise ratio maps were built (Figure 3) for the set of τ. As the signal value, we take the variance of $F_\tau^{\mathrm{hf}}(t_i)$ for each box. As the noise value, the variance of the emission intensity from a remote box is taken. This box is marked by a square in the lower left corner of the map. Contours show the levels 0.1, 0.3, 0.5, 0.7, 0.9, and 0.97 of $F^{\max}$. Here $F^{\max}$ is maximal flux at the time $t_{73} = 02{:}14{:}53$ UT. It is seen that significant pulsations, with a signal-to-noise ratio greater than at least 4, occupy the compact area within contour $F(t_i) \geq 0.1\ F_{\max}$. This indicates that they belong to the flaring radio loop. Boxes within the mentioned level are then used for a subsequent detailed study.

4.3. Position of Sources of Different Spectral Components

For each box, autocorrelation functions of the modulation depth $\Delta_\tau(t_i)$ (Equation (2)) are calculated for the set of τ and their periodograms are built. Periods of all spectral components in the periodograms are then considered for all boxes. In some groups of boxes there is a quite similar set of periodicities. The list of those periods is presented in Table 1. In

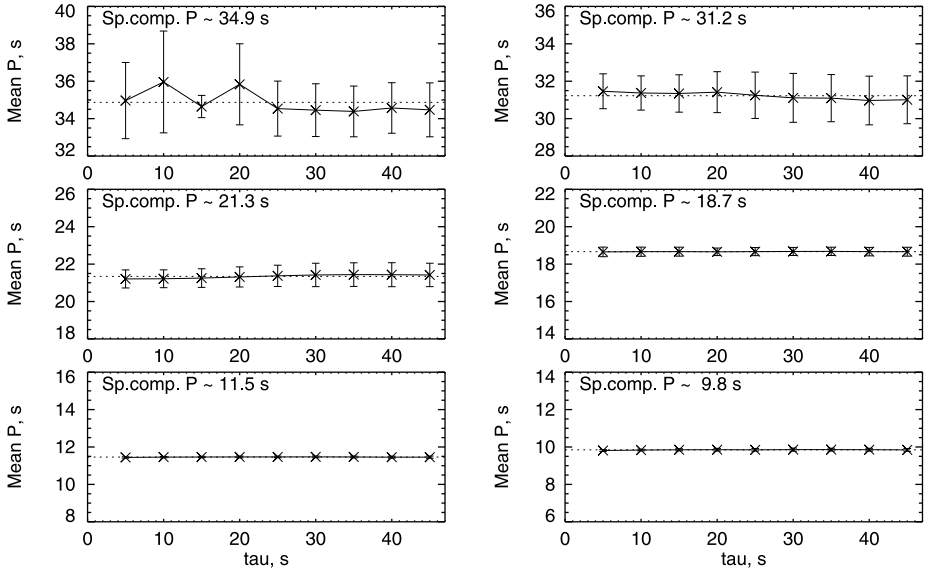

Figure 4 The mean periods of the significant QPPs with periods of 34.9 s, 31.2 s, 21.3 s, 18.7 s, 11.5 s, and 9.8 s *versus* smoothing filter width τ. The vertical axes represent values of the periods $\langle P\rangle$ in seconds; the horizontal axes represent values of τ in seconds. The mean period $\langle P\rangle$ for each spectral component and for each τ is obtained only over those boxes where the spectral component power is higher than the significance level $W > W_{\rm sign} \approx 11.4$. Mean values of periods $\langle P\rangle$ are marked by crosses; error bars show the standard deviations from the mean period. The dashed line represents the average period value over all τ.

Table 1, the first and second columns are the number and notation of a spectral component. The third column shows period limits within which spectral peaks are sought. The fourth column presents mean values of periods $\langle P\rangle$ of spectral components and their uncertainties (errors) ΔP. The uncertainties are mainly caused by the discreteness of the period grid in the Fourier transform. Note that in many boxes peaks appear in pairs with slightly different periods: $\langle P\rangle_1^{\rm I} \approx 34.9$ s and $\langle P\rangle_2^{\rm I} \approx 31.2$ s, $\langle P\rangle_1^{\rm II} \approx 21.3$ s and $\langle P\rangle_2^{\rm II} \approx 18.7$ s, $\langle P\rangle_1^{\rm III} \approx 11.5$ s and $\langle P\rangle_2^{\rm III} \approx 9.8$ s. Signals from some boxes also have various combinations of rather weak spectral peaks with periods $\langle P\rangle_3 \approx 16.4$ s, $\langle P\rangle_4 \approx 13.3$ s, $\langle P\rangle_5 \approx 12.3$ s.

It is interesting that almost the same set of spectral components is seen in the periodograms of HXR emission intensity at 6 – 12 keV, obtained using data from the RHESSI satellite (Figure 1d and the last column of Table 1). Spectral components with periods $\langle P\rangle_2^{\rm I}$, $\langle P\rangle_1^{\rm II}$ have their equivalents in the NoRH spatially unresolved signal (Figure 1c and the fifth column of Table 1). The notation $\langle P\rangle$ in the two last columns means the average value over the τs.

Kupriyanova *et al.* (2010) used several criteria to distinguish between periodicities that belong to a signal and periodicities that are artifacts of the mathematical processing. One criterion is the independence of the period of a spectral component on the smoothing filter width τ. We also have checked the stability of the periods. Figure 4 shows the dependence of the mean-over-image values of periods of the spectral components *versus* τ. For each spectral component and each τ, the mean periods are calculated only over those boxes where the spectral component power exceeds the significance level, $W > W_{\rm sign} \approx 11.4$. The mean values of periods $\langle P\rangle$ are marked by crosses. Error bars show the standard deviations from the mean value. The dashed line represents the average period over all intervals of τ. Figure 4

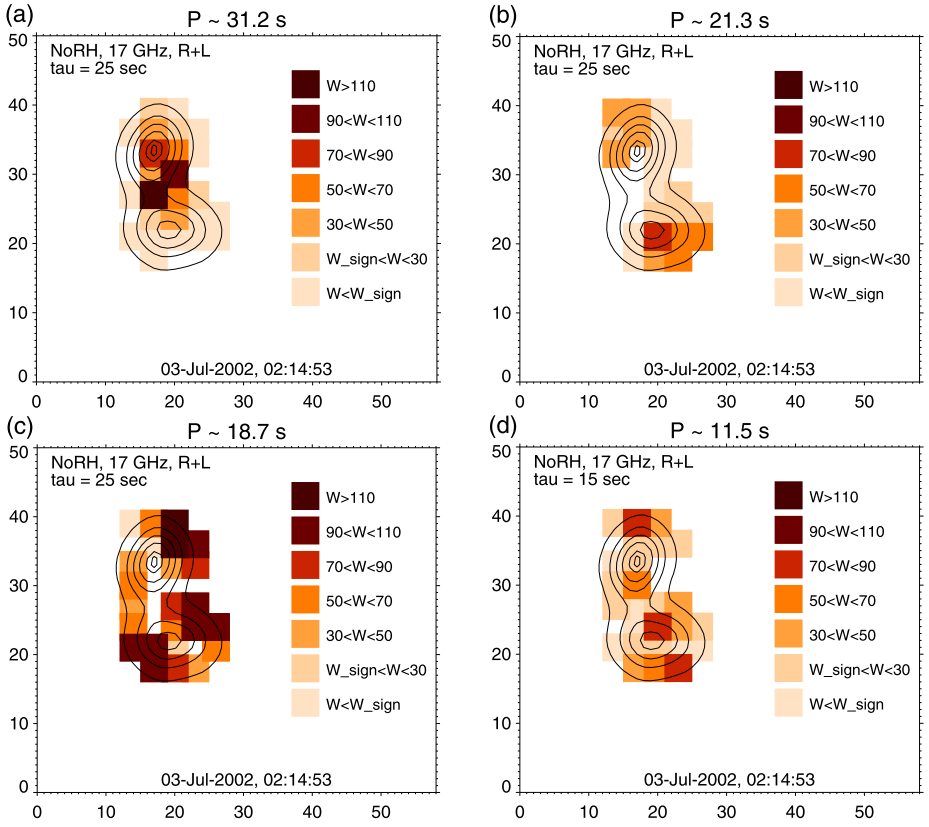

Figure 5 (a) – (d) Spatial distribution of the spectral power W of the four strongest spectral components with average periods of 31.2 s, 21.3 s, 18.7 s and 11.5 s for smoothing intervals $\tau = 25$ s and $\tau = 15$ s. The horizontal and vertical axes represent the number of pixels, 1 pixel $\approx 2.5''$. The discrete scale from dark to light refers to the decreasing values of the normalized spectral power of pulsations. Contours show the levels 0.1, 0.3, 0.5, 0.7, 0.9, and 0.97 of $F^{\max}$ at the time $t_{73} = 02{:}14{:}53$ UT. Here $F^{\max}$ is maximal over the entire image intensity at t_{73}.

shows that the largest scattering occurs for periods of the spectral component $\langle P \rangle_1^{\mathrm{I}} \approx 34.9$ s. Nevertheless, its average error through all intervals τ is held within the error bar presented in Table 1. Periods of the other spectral components are more stable to changes of τ. Their standard deviations from a mean period through the set of τ are much less than the error bars defined by the period grid.

The spatial distributions of spectral powers of the four most powerful spectral components are displayed in Figure 5a – d. These figures are the most interesting results of our QPP spatial structure analysis. One can see that the spectral power W of the spectral components is distributed nonuniformly throughout the flaring area. From Figure 5a it is clear that QPPs with period of $\langle P \rangle_2^{\mathrm{I}}$ occupy a compact area between the northern and southern sources, closer to the northern source. Pulsations with period $\langle P \rangle_{1,2}^{\mathrm{II}}$ have their maximum amplitude mainly in the outer parts of the northern and southern radio sources associated with the footpoints of the flaring loop (Figures 5b – c). QPPs with period of $\langle P \rangle_1^{\mathrm{III}}$ reach their maximal power in three sites: between the sources and in the outer parts of both sources.

4.4. Properties of QPPs from Different Positions in the Flaring Loop

To increase the signal-to-noise ratio, we merged areas with similar profiles of the wavelet spectra into three large boxes: 8×8 pixels $\approx 20'' \times 20''$ (Figure 6a). Time profiles of modulation depth $\Delta_\tau(t_i)$ from these boxes for $\tau = 25$ s are shown in Figure 6b. They present a good quality of oscillatory patterns through the whole time interval. The periodic structure of these time profiles is much better seen in its autocorrelation functions (Figure 6c). Hence, pulsations keep the phase during a sufficiently long time and have rather good quality: $Q = \pi n \approx 20$ (n is the number of periods) for QPPs with $P \approx 30$ s and $Q \geq 30$ for QPPs with $P \approx 20$ s. Note that the emission intensity oscillates in anti-phase in the northern and southern sources (Figure 6b).

Wavelet spectra of $\Delta_\tau(t_i)$ from the selected three large boxes are shown in Figure 6d for the smoothing filter width $\tau = 25$ s. In the outer parts of the flaring region, the shapes of the wavelet spectra are quite similar. The areas above the northern source (box 0) and in/under the southern source (box 2) are characterized by dominant QPPs with period $P_2^{\rm II} \approx 19$ s at the beginning of the final phase and QPPs with period $P_1^{\rm II} \approx 21$ s at its end. Also, there is a weak maximum at $P_1^{\rm I} \approx 34-37$ s. Above the northern source (box 0), all three components are equally powerful. Under the southern source (box 2), the spectral component with period $P_1^{\rm I} \approx 34-37$ s is less powerful than that above the northern one. The wavelet spectrum for box 1 keeps its shape for a range of positions of its center, from the bottom of the northern source down to the middle between the two sources. Interestingly, the periods of both spectral components here are smaller than at the periphery: $P_2^{\rm I} \approx 29-30$ s, $P_2^{\rm II} \approx 17$ s. In the inner region, QPPs with period $P_2^{\rm I}$ are predominant. The component with period $P_2^{\rm II}$ is significantly weaker. Note that the wavelet spectra for boxes 0 and 2 have a weak component with period $P^{\rm III} \approx 10$ s. It is more pronounced at lower τ. In box 1, however, this component is weaker than in boxes 0 and 2, for all τs.

Note that the stability of the periodicities in the wavelet spectra is noticeably lower than would be expected from the modulation depth time profiles and its autocorrelation functions (see Figures 6b, c).

Results of the Fourier analysis for the large boxes confirm the results of the wavelet analysis. Periodograms of autocorrelation functions R of modulation depth $\Delta_\tau(t_i)$ for the set of τs are shown in Figure 6e by solid lines. The periodograms for boxes 0 and 2 have similar profiles. They indicate the following set of mean periods: $P_1^{\rm I} \approx 32.6 \pm 3.0$ s, $P_1^{\rm II} \approx 22.0 \pm 1.5$ s, $P_2^{\rm II} \approx 18.8 \pm 1.0$ s, $P_1^{\rm III} \approx 11.5 \pm 0.4$ s, and $P_2^{\rm III} \approx 9.8 \pm 0.3$ s. Periodograms for box 1 show a dominant spectral peak with period $P_1^{\rm I} \approx 30.3 \pm 3.0$ s. Also, there are three very weak peaks with periods from 13.1 s to 17.7 s, which are slightly higher than the significance level only for $\tau \leq 15$ s. These values are summarized in Table 2. Those spectral components which are present in the periodograms but with a significance level lower than 95 % are indicated in italics.

The results for the three large boxes are in good agreement with the results of the correlation analysis for the small boxes presented in the previous subsection. The small difference in values of the spectral component No. 1 (compare Tables 1 and 2) can be caused by the fact that the large boxes occupy areas with pulsations with slightly different periods. Integration of these periods can lead to a slight shift of its mean value.

In contrast to the integral signal (Figure 1b), the wavelet analysis of signals from individual parts of the flaring region shows the absence of any drifting periods. A comparison of Figure 2c and Figures 6d – e shows that the flux from the southern source (the thick line in Figure 2c) with QPPs of period $P^{\rm II}$ dominates at the beginning of the time interval under analysis. In the middle part of the time interval, the flux from the northern source with QPPs

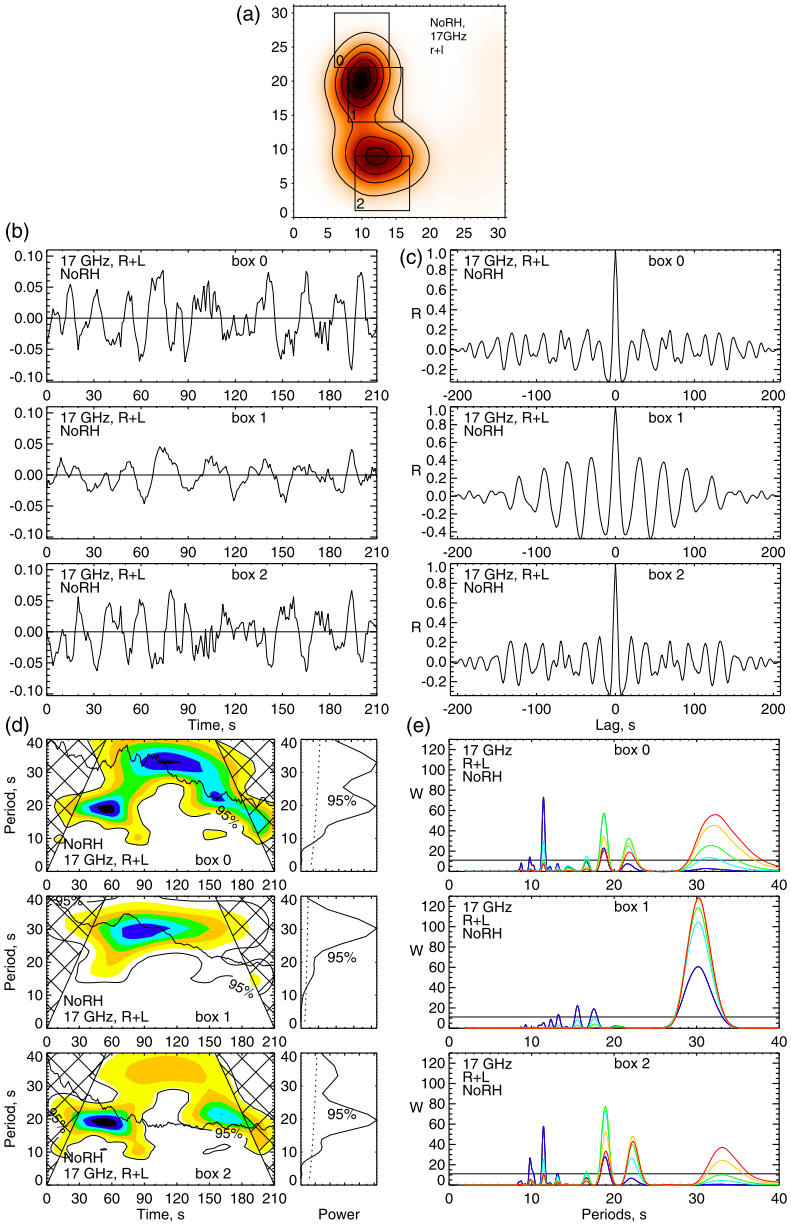

Figure 6 (a) The distribution of radio brightness at $t_{73} = 02{:}14{:}53$ UT. Contours show the levels 0.1, 0.3, 0.5, 0.7, 0.9, and 0.97 of $F^{\max}$. Numbered squares show the positions of three large boxes of $20'' \times 20''$. Panels (b – d) are for $\tau = 25$ s. (b) Time profiles of modulation depth $\Delta_\tau(t_i)$ from these boxes (02:13:40 to 02:17:10 UT). (c) Autocorrelation functions R of $\Delta_\tau(t_i)$. (d) Wavelet power spectra (WPS) of $\Delta_\tau(t_i)$. Thick black curve shows the normalized temporal profiles of the fluxes from each box. Cross-hatched regions on the ends of the WPS indicate the cone of influence. The small panel on the right of the WPS represents the global WPS. (e) Periodograms of autocorrelation functions R of $\Delta_\tau(t_i)$. The blue, pale blue, green, orange, and red solid lines correspond to the set of smoothing times $\tau = 15$, 20, 25, 30, and 35 s. The horizontal line marks the significance level $W_{\text{sign}} \approx 11.4$.

Table 2 List of the periods for large boxes.

No.	Box 0 $\langle P\rangle \pm \Delta P$, [s]	Box 1 $\langle P\rangle \pm \Delta P$, [s]	Box 2 $\langle P\rangle \pm \Delta P$, [s]
1	32.1 ± 3.0	–	33.0 ± 3.0
2	–	30.3 ± 3.0	–
3	21.8 ± 1.5	–	22.2 ± 1.5
4	18.8 ± 1.0	–	18.9 ± 1.0
5	–	*17.7 ± 0.7*	–
6	–	*15.5 ± 0.6*	*15.1 ± 0.6*
7	*13.1 ± 0.5*	–	13.1 ± 0.5
8	11.4 ± 0.4	–	11.5 ± 0.4
9	9.8 ± 0.3	–	9.8 ± 0.3

of period P^{I} becomes stronger (the thin line in Figure 2c). Therefore, we conclude that the drift observed in the spectrum of the integral signal is due to a gradual redistribution of the radio brightness from the external source to the internal one.

4.5. Beating of Oscillations with Close Periods

Our periodogram analysis shows that the set of three pairs of strong spectral components, $\langle P\rangle_1^{\mathrm{I}} \approx 34.9$ s and $\langle P\rangle_2^{\mathrm{I}} \approx 31.2$ s, $\langle P\rangle_1^{\mathrm{II}} \approx 21.3$ s and $\langle P\rangle_2^{\mathrm{II}} \approx 18.7$ s, $\langle P\rangle_1^{\mathrm{III}} \approx 11.5$ s and $\langle P\rangle_2^{\mathrm{III}} \approx 9.8$ s, is observed throughout the analyzed time interval (02:13:40 – 02:17:10 UT) (see Section 4.3). It is obvious from the wavelet spectra that the intensity of individual spectral components varies with time (Section 4.4). This is especially evident for the second spectral component ($\langle P\rangle^{\mathrm{II}} \approx 19-21$ s). Its intensity at the beginning of the interval was large, and then greatly reduced, and finally it increased again.

This temporal behavior of the spectral components suggests that the effect of beating of signals with close periods is very probable in this flaring region. Indeed, under the influence of multiple MHD oscillations in the region, some of the characteristics of the radio source (*e.g.*, a distribution of nonthermal electrons, a magnitude and/or direction of the magnetic field, or a plasma density) may also oscillate. This leads to modulations of the gyrosynchrotron emission received by NoRH from an oscillating source (or sources) located in the direction inside the NoRH main beam. Let us consider this type of impact, without specifying its nature, but simply setting certain modeling periodic functions.

Generally, the model function is defined as a time series of length N. In accordance with the NoRH data for the decay phase of the flare on 3 July 2002, $N = 211$ has been chosen. The total signal function has been given as a superposition of a low-frequency background F_{bkgr}, a periodic signal F_{per}, and a noise F_{noise} function:

$$F(t_i) = F_{\mathrm{bkgr}}(t_i)\big(1 + F_{\mathrm{per}}(t_i)\big) + F_{\mathrm{noise}}(t_i), \tag{4}$$

$i = 0, 1, \ldots, N-1$. Here $F_{\mathrm{bkgr}} = A_s \cos(2\pi t_i / P_{\mathrm{bkgr}} - \varphi_{\mathrm{bkgr}})$ is the periodic background function with amplitude A_s, period P_{bkgr}, and phase φ_{bkgr}. The periodic component has been defined as the superposition of sinusoids with periods P_α, phases φ_α, and amplitude A_α, $0 < A_\alpha < 1$:

$$F_{\mathrm{per}}(t_i) = \sum_{\alpha=1}^{m} A_\alpha \sin\left(\frac{2\pi t_i}{P_\alpha} - \varphi_\alpha\right).$$

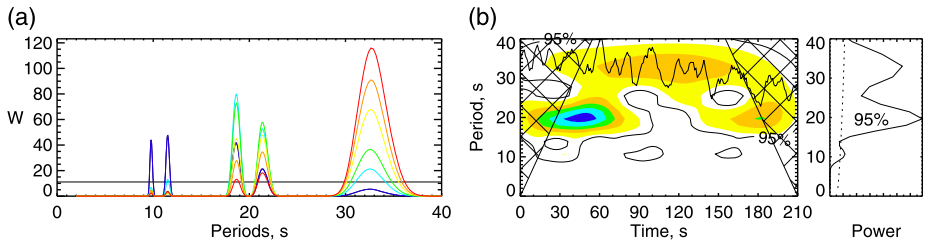

Figure 7 (a) Periodograms of autocorrelation functions for the set of modeled time series of the modulation depth $\Delta_{m\tau}$. The horizontal axis represents periods in seconds, and the vertical axis the spectral power W. The periodogram for $\tau = 15$ s is colored in blue, for $\tau = 20$ s in pale blue, for $\tau = 25$ s in green, for $\tau = 30$ s in yellow, for $\tau = 35$ s in orange, for $\tau = 40$ s in red. (b) The colored panel shows the wavelet spectrum of the modeled time series $\Delta^m_\tau(t_i)$ for $\tau = 25$ s. The superimposed normalized temporal profile of the radio flux is shown by the thick black curve.

The noise function $F_{\rm noise}$ has been set as a time series of normally distributed random quantities with standard deviation A_n and with mean value 0. The amplitudes A_α, A_n, periods P_α, and phases φ_α, $\varphi_{\rm bkgr}$ can be varied in order to find their optimal values.

The model function is then transformed into a set of time series of the modulation depth $\Delta^m_\tau(t_i)$ for different smoothing intervals τ by the procedure that was used for the real NoRH data analysis (see Equation (2)). Then, their autocorrelation functions, periodograms, and wavelet spectra are calculated.

The model function is defined as follows. The periodic component is a superposition of six sinusoids with periods derived from observations: $P^{\rm I}_1 = 34.9$ s, $P^{\rm I}_2 = 31.2$ s, $P^{\rm II}_1 = 21.3$ s, $P^{\rm II}_2 = 18.7$ s, $P^{\rm III}_1 = 11.5$ s, $P^{\rm III}_2 = 9.8$ s. Their amplitudes and phases (in radians) were chosen as $A^{\rm I}_1 = A^{\rm I}_2 = A^{\rm II}_1 = A^{\rm II}_2 = 0.1$, $A^{\rm III}_1 = A^{\rm III}_2 = 0.08$, $\varphi^{\rm I}_1 = 2.5$, $\varphi^{\rm II}_1 = 2.9$, $\varphi^{\rm II}_1 = 5.8$, $\varphi^{\rm I}_2 = \varphi^{\rm II}_2 = \varphi^{\rm III}_2 = 0$. All six sinusoids exist throughout the whole time interval. Parameters of the background are set as: $A_s = 1$, $P_{\rm bkgr} = 3N$, and $\varphi_{\rm bkgr} = 0$. The amplitude of the noise component is $A_n = 0.1$.

Periodograms of the autocorrelation functions for the set of modeled time series are presented in Figure 7a. The graphs show that the components $P^{\rm I}_1$ and $P^{\rm I}_2$ are not resolved as individual spectral peaks. Instead of two peaks, only one smooth broad peak with the average (over τ) period $P^{\rm I} \approx 32.6 \pm 3.0$ s is seen. The periods of the other sinusoids are clearly defined on the periodograms: $P^{\rm II}_1 = 21.3 \pm 1.5$ s, $P^{\rm II}_2 = 18.6 \pm 1.5$ s, $P^{\rm III}_1 = 11.5 \pm 0.4$ s, $P^{\rm III}_2 = 9.8 \pm 0.3$ s.

Results of the wavelet analysis of the model function are shown in Figure 7b. Although sinusoids constituting the periodic component of the model function are defined through the whole time interval, we do not see continuous stripes in the wavelet spectrum. Instead, the individual islands are seen at the levels of $P^{\rm I} \approx 30$ s, $P^{\rm II} \approx 20$ s, and $P^{\rm III} \approx 10$ s. The appearance of the gaps is explained by the beating of sinusoids with close periods. The beating between the sinusoids $P^{\rm I}_1$ and $P^{\rm I}_2$ occurs with period $P^{\rm I}_b \approx 570$ s. They amplify each other in the middle of the time interval. As a result, the wavelet spectrum (Figure 7a) has its spectral maximum at a period of about 30 s at time $t \approx 105$ s. The beating period between the sinusoids with periods $P^{\rm II}_1$ and $P^{\rm II}_2$ is $P^{\rm II}_b \approx 306$ s. After about 100 s from the beginning, these sinusoids damp each other, oscillating in anti-phase. Hence, the wavelet spectrum shows the absence of significant oscillations with periods of about 20 s at time $t \approx 100$ s. The interference between the sinusoids with periods $P^{\rm III}_1$ and $P^{\rm III}_2$ leads to the appearance of a series of islets at periods of about 10 s, which are pronounced more clearly in the wavelet spectra for the lower smoothing intervals τ. Therefore, the effect of beatings of signals with close periods explains the apparent low quality of the QPPs in their wavelet spectra.

A comparison of the wavelet spectrum of the model signal (Figure 7b) with the spectrum of the real signal (Figure 6d) shows a very good agreement. This confirms our initial idea that the beating between real signals can adequately describe the observed properties of the wavelet spectra shown in Figure 6d. Note that a further understanding requires finding specific mechanisms of QPPs in the flaring region.

5. Discussion

The physical origin of the observed pulsations in the microwave emission during flares may be the presence of MHD oscillations of coronal magnetic loops. These oscillations can lead to a modulation of the acceleration of the emitting electrons or to the modulation of the efficiency of the gyrosynchrotron emission of these electrons due to quasi-periodic variations of the plasma density and/or the strength and direction of the magnetic field (Nakariakov and Melnikov, 2009; Mossessian and Fleishman, 2012).

5.1. MHD Oscillation Modes in the Observed Flare Loop

According to the theory developed by Zaitsev and Stepanov (1975, 2008), Edwin and Roberts (1983), and Nakariakov and Verwichte (2005), the dispersion equation for eigen oscillatory modes in a straight homogeneous cylinder is written as follows:

$$\rho_e\left(v_{\rm ph}^2 - v_{Ae}^2\right)\mu_0 \frac{Z'_m(\mu_0 a)}{Z_m(\mu_0 a)} + \rho_0\left(v_{A0}^2 - v_{\rm ph}^2\right)\mu_e \frac{Z'_m(\mu_e a)}{Z_m(\mu_e a)} = 0. \tag{5}$$

Here $v_{\rm ph} = \omega/k$ is the phase velocity, ω, k are the frequency of oscillations and its wave vector along the loop axis, a is the radius of the loop cross section, ρ_α is the plasma density, $v_{A\alpha}$ is the Alfvén velocity, μ_α is the radial wave number

$$\mu_\alpha^2 = k^2 \frac{(c_{s\alpha}^2 - v_{\rm ph}^2)(v_{A\alpha}^2 - v_{\rm ph}^2)}{(c_{s\alpha}^2 + v_{A\alpha}^2)(c_{T\alpha}^2 - v_{\rm ph}^2)}, \tag{6}$$

$c_{T\alpha} = v_{A\alpha} c_{s\alpha}/\sqrt{v_{A\alpha}^2 + c_{s\alpha}^2}$ is the tube velocity, $Z'_m(x) = {\rm d}Z_m(x)/{\rm d}x$, $Z_m(x)$ is the cylinder function of m order (m is integer), $\alpha = 0, e$ refers to the plasma inside and outside a loop. The order m of cylinder functions determines the type of oscillatory mode. So $m = 0, 1, 2, 3$ refers to the radial (sausage), kink, and ballooning (flute) modes.

Conditions for the existence of the MHD modes as well as their characteristics are very sensitive to plasma parameters (magnetic field B_α, number density n_α, temperature T_α) inside and outside a loop, as well as to the radius-to-length ratio of a loop. This makes the MHD oscillations a good tool for diagnostics of the flaring plasma. But before we exploit this possibility, we should identify a specific oscillatory mode responsible for the observed QPPs in the flaring loop.

To identify the specific MHD mode, we use Equations (5) – (6) and the flaring loop parameters derived in Section 4. Then we calculate possible periods of standing waves for the basic MHD modes: acoustic, kink, sausage, and ballooning. For estimates of pulsation periods corresponding to different MHD modes, we assumed the following ranges of parameter variations in the flaring loop plasma: $B_0 = 70-200$ G, $T_0 = (2-6)\cdot 10^6$ K, $n_0 = 10^{10}-10^{11}$ cm^{-3}, $B_e = (1.01-1.3)B_0$, $T_e = 10^6$ K, $n_e = (0.1-0.5)n_0$. The loop length $L \approx 35000$ km and the radius-to-length ratio of the loop $a/L \approx 0.2$ were taken from the

spatial observations (see Section 4.1). The period of a standing MHD mode is defined by the loop length and the phase velocity of the mode:

$$P = 2L/nv_{\rm ph}, \tag{7}$$

where n is a harmonic number.

Our calculations have shown that the acoustic modes with phase velocity $v_{\rm ph} = c_{s0}$ provide oscillations with periods significantly greater than those observed in the flare on 3 July 2002. Even at temperature $T_0 = 7 \times 10^6$ K, the periods of the fundamental, second, and third harmonics are obtained to be $P_s^{\rm I} \approx 165$ s, $P_s^{\rm II} \approx 82$ s, and $P_s^{\rm III} \approx 52$ s, respectively. Therefore, the acoustic mode cannot be responsible for the observed pulsations.

The assumption of the sausage mode as the origin of the oscillations agrees well with the spatial distribution of the observed spectral components (Figures 5a – d). Indeed, the position of the spectral component $P \approx 30$ s (Figure 5a) between the northern and southern sources (loop footpoints) is well explained by the modulation of the gyrosynchrotron radio emission by the global sausage mode, because in this case the maximal amplitude of the magnetic field oscillation is located in the loop top (Nakariakov, Melnikov, and Reznikova, 2003). The position of the maximal amplitude of the component with $P \approx 20$ s in the loop legs close to the footpoints (Figures 5b, c) is well explained by the second harmonic of the sausage mode. The nodes of the second harmonic are located in the footpoints and in the loop top, and the amplitude of the oscillations reaches its maximum between the loop top and each of the footpoints. However, a detailed analysis of the dispersion equation (see Equation (5)) shows that the fundamental (global) mode of sausage oscillations cannot exist in as thin a loop as the observed one (with $a/L \leq 0.2$). The problem is that the trapped global sausage mode can exist only for values of the wave number larger than the critical value $k > k_c$ (Nakariakov, Melnikov, and Reznikova, 2003),

$$k_c = \frac{2.4}{a}\sqrt{\frac{(c_{s0}^2 + v_{Ae}^2)(v_{Ae}^2 - c_{T0}^2)}{(v_{Ae}^2 - v_{A0}^2)(v_{Ae}^2 - c_{s0}^2)}}. \tag{8}$$

The second and third harmonics cannot provide the observed ratio of periods. Even with too high a value of the plasma density ($n_0 = 10^{11}$ cm^{-3}) and the low value of the magnetic field ($B_0 = 70$ G), the periods of the second and third harmonics are too close to each other and their ratio is $P_{\rm rad}^{\rm II}/P_{\rm rad}^{\rm III} \approx 26$ s/23 s ≈ 1.13. Note that from observations we have ratios $P_{\rm obs}^{\rm I}/P_{\rm obs}^{\rm II} \approx 31.1$ s/18.7 s ≈ 1.66 and $P_{\rm obs}^{\rm II}/P_{\rm obs}^{\rm III} \approx 18.7$ s/11.4 s ≈ 1.64; these values are considerably greater than that calculated for the sausage mode.

Our calculations show that the kink mode provides values of the periods and their ratios much closer to those observed. For $B_0 = 180$ G, $T_0 = 5 \times 10^6$ K, $n_0 = 5 \times 10^{10}$ cm^{-3} we have $P_{\rm kink}^{\rm I}/P_{\rm kink}^{\rm II} \approx 31.1$ s/16.8 s ≈ 1.64 and $P_{\rm kink}^{\rm II}/P_{\rm kink}^{\rm III} \approx 16.8$ s/11.7 s ≈ 1.43. Note that, for these plasma parameters, the fundamental and second harmonics of the sausage mode do not exist at all, and the period of its third harmonic is too small, $P_{\rm rad}^{\rm III} \approx 7.5$ s.

5.2. Mechanisms of Microwave Emission Modulation by Kink Oscillations of a Flare Loop

Let us consider now possible mechanisms of the microwave emission modulation by the kink mode oscillations of the flare loop. A well-known mechanism is the gyrosynchrotron emission modulation produced by horizontal kink mode oscillations. During this type of oscillation, the magnetic field strength is almost unchanged, but the direction of the field lines can change remarkably. The modulation occurs due to the dependence of the emissivity

of the nonthermal gyrosynchrotron radiation on the angle θ between the magnetic field direction in the source and the line of sight (Dulk and Marsh, 1982):

$$I(\theta) \propto (\sin\theta)^{-0.43+0.65\delta} B^{0.90\delta-0.22}. \tag{9}$$

Here δ is the spectral index of accelerated electrons, $2 < \delta < 7$, and B is the magnetic field strength.

In our case the flaring loop is oriented in the north-south direction and its heliographic coordinates are $S19W48$. Thus, field lines near the footpoints are probably inclined by more than 48° to the line of sight for the northern footpoint and less than 48° for the southern footpoint. The looptop field lines are inclined at an angle of the order of 70°. This means that in order to produce the observed oscillations of 2 % to 5 % of the microwave intensities near the footpoints and looptop (see Figure 6), the amplitude of the angle should be around $\Delta\theta = 1.5-3.0°$, assuming $\delta = 4.7$. Such angle variations look rather reasonable.

It follows from Equation (9) and properties of the horizontal kink mode that the modulation of the gyrosynchrotron emission by the fundamental (global) kink mode with period $P \approx 30$ s can be significant throughout the loop. The QPPs are expected to be in phase everywhere in the loop. The QPPs with period $P \approx 20$ s caused by the second harmonic of the kink mode are expected to have larger amplitudes at the position between the loop top and footpoints, but closer to the footpoints. These oscillations of the emission intensity should be in anti-phase in the northern and southern sources because of the anti-phase displacements of the opposite loop legs (see Nakariakov and Verwichte, 2005). In general, this behavior of the predicted microwave emission is in agreement with the observed properties of QPPs discussed in Section 4. Especially good agreement is found for the footpoints of the flaring loop where viewing angle variations are expected to be maximal both for $P \approx 30$ s and $P \approx 20$ s oscillations (see Figure 6).

Another mechanism of gyrosynchrotron modulation by kink oscillations can be provided by the vertical oscillations of a magnetic loop. The first observations of this oscillatory mode by the *Transition Region and Coronal Explorer* (TRACE) spacecraft in the 195 Å bandpass were reported by Wang and Solanki (2004). Theoretical studies of the mode were reported in a number of papers (Verwichte, Foullon, and Nakariakov, 2006; Diaz, 2006; Tsap *et al.*, 2008, *etc*). Recently, using data from the *Atmospheric Imaging Assembly* (AIA) and the *Helioseismic and Magnetic Imager* (HMI) on board the *Solar Dynamics Observatory* (SDO) together with the *Solar Terrestrial Relations Observatory* STEREO/EUVI-A, Aschwanden and Schrijver (2011) found that vertical kink oscillations of a magnetic loop with curvature radius variations $R(t) = R_0 + A(t)$ can modulate the plasma density and magnetic field strength in the oscillating loop more or less similarly to the sausage mode oscillations, but with a different period. When the loop stretches up or shrinks down, its cross-sectional radius $a(t)$ varies proportionally to the oscillating amplitude $A(t)$ (see Equation (7) in the paper of Aschwanden and Schrijver, 2011). In our notation,

$$a(t) = a_0\left(1 + \frac{A(t)}{R_0}\right). \tag{10}$$

This results in periodic changes of the loop volume and provides plasma density variations inversely to $a(t)$. On the other hand, from the law of magnetic flux conservation, it follows that the magnetic field strength should also vary inversely to $a(t)$. The strongest variations of the magnetic field $B(t)$ are expected in the loop top for the case of the global vertical kink mode.

As follows from Equation (9), the intensity of gyrosynchrotron emission is proportional to the magnetic field to the power of four, $I \propto B^4$, for $\delta = 4.7$. Obviously, this effect can lead

to a strong modulation of the gyrosynchrotron emission in the upper part of the loop, which is exactly what we observe for the 30 s spectral component (see Figure 5a). A calculation of the modulation depth using Equations (1) and (2) gives its value in the loop top: $\Delta I/I < 5\ \%$. Therefore, the variations of the magnetic field should be as low as $\Delta B/B = \Delta I/4I < 1.25\ \%$.

From the law of magnetic flux conservation $B(t) \times S(t) = const$, where $S(t) = \pi a(t)^2$, we conclude that variations of the loop cross-sectional radius $a(t)$ are twice less than variations of the magnetic field and anti-correlate with them; $\Delta a/a_0 = -\Delta B/2B$, that is $\Delta a/a_0 < 0.6\ \%$. From Equation (10) one gets $\Delta a/a = A/R_0$. For the fundamental kink mode, variations of a have maximum amplitude in the loop top. An analysis of the loop spatial structure (Section 4.1) gives the following estimations for the loop cross-sectional radius and for the loop curvature radius, respectively: $a \approx 4$ pixels and $R = d/2 \approx 7.5$ pixels. This means that the variations of these sizes are very small, $\Delta a < 0.024$ pixels and $A < 0.045$ pixels. These changes are considerably less than the NoRH beam size, and cannot be observed directly. But they are high enough to produce observable changes in fluxes from different sites of the flaring region.

Similar considerations of the second and third harmonics of the vertical kink mode oscillations lead to the following predictions. The second harmonic should provide anti-phase oscillations of the magnetic field strength in the opposite ends of the flaring loop and, consequently, the anti-phase oscillations of the gyrosynchrotron microwave emission. The third harmonic has three regions of high-amplitude variations of the magnetic field and corresponding regions of microwave emission variations: one in the middle and two near the ends of the magnetic loop. These predictions are in good agreement with our results of spatially resolved observations as shown in Figure 5. However, note that the theory of the vertical kink mode oscillations is still in the initial stage of its development, and more efforts by MHD theoreticians are needed to achieve more reliable conclusions.

5.3. Spectral Components with Close Periods

In Sections 4.3 – 4.5 we considered observations of the spectral components with close periods. According to our estimations from observations, the difference between periods is $\Delta P^{\mathrm{I}}/P^{\mathrm{I}} = 2(P_1^{\mathrm{I}} - P_2^{\mathrm{I}})/(P_1^{\mathrm{I}} + P_2^{\mathrm{I}}) \approx 0.13$ for the component with period $P^{\mathrm{I}} \approx 30$ s. For the component $P^{\mathrm{II}} \approx 20$ s we have the same value, $\Delta P^{\mathrm{II}}/P^{\mathrm{II}} \approx 0.13$. In principle, the pairs of QPPs with close periods may be caused by the existence in the loop, along with the kink mode, of other modes with close phase velocities, such as the ballooning mode, or the torsional mode. For example, for the ballooning mode ($m = 2$), we obtain almost the same ratios of periods between the fundamental, second, and third harmonics as for the kink mode if we take the following parameters in the magnetic loop: $B_0 = 180$ G, $T_0 = 5 \times 10^6$ K, $n_0 = 5 \times 10^{10}$ cm^{-3}. However, the periods of the ballooning mode ($P_{\mathrm{fl2}}^{\mathrm{I}} \approx 30.6$ s, $P_{\mathrm{fl2}}^{\mathrm{II}} \approx 15.7$ s, $P_{\mathrm{fl2}}^{\mathrm{III}} \approx 10.8$ s) differ from the periods of the kink mode only by $\Delta P \approx 1$ s. This difference is too small ($\Delta P/P = 0.03$) to provide the observed difference between close periods. Also, the effect of beating that is seen in the wavelet spectra (Figure 6d) cannot be explained in terms of the joint existence of the kink and ballooning modes in the same single loop.

The simultaneous existence of both horizontal and vertical kink oscillations in a single magnetic loop could also, in principle, provide two spectral components with close but different periods since these modes may have slightly different phase velocities (Verwichte, Foullon, and Nakariakov, 2006). Unfortunately, so far we do not know of publications where the phase velocities of horizontal and vertical modes are compared for the case of the same magnetic loop.

The above-mentioned equality $\Delta P^{\mathrm{I}}/P^{\mathrm{I}} = \Delta P^{\mathrm{II}}/P^{\mathrm{II}} \approx 0.13$ suggests another possibility for the existence of pairs of spectral components with such different periods. They can be produced by two adjacent thin kink-oscillating loops with slightly different lengths L_1 and L_2. The rather wide NoRH beam at 17 GHz ($\Delta\phi \geq 10''$) can include sections of both thin loops simultaneously, so the NoRH signal can be modulated by oscillations of both loops with slightly different periods. The idea of the existence of two adjacent kink-oscillating loops with close periods is supported by recent observations with the *AIA* instrument onboard *SDO* in the EUV filter line 171 Å (Aschwanden and Schrijver, 2011). The loops were excited in phase but the secondary loop had an oscillation period about 10 % shorter than the primary one. Note that MHD modelling also suggests that interacting loops can give solutions different from the solution of a single loop. For example, Van Doorsselaere, Ruderman, and Robertson (2008) analytically considered a system of two adjacent identical kink-oscillating loops and showed that the system generates two spectral components with different but close periods.

6. Conclusions

The flare on 3 July 2002 was registered using NoRH with high angular ($10''$ at 17 GHz) and temporal (up to 100 ms) resolution and showed interesting QPP properties. Using methods of correlation and Fourier analysis of the integrated signal (correlation amplitudes) Kupriyanova *et al.* (2010) found QPPs with periods of $P \approx 20$ s and $P \approx 30$ s. At the same time, wavelet analysis showed the presence of only one spectral component, but with a drift of the period from $P \approx 20$ s up to $P \approx 30$ s.

In order to explore the spatial structure of these QPPs, radio maps were built with a time step of 1 s using NoRH data at 17 GHz. Then a correlation, Fourier and wavelet (Morlet) analysis of the varying signal from each small part (box with size $10''$) of the radio map was carried out. The analysis of the QPP spatial structure showed that, in contrast to the integrated signal (Figure 1b), no oscillations with drifting period were observed throughout the flaring area. Instead of one spectral component with a drifting period, pulsations with two almost constant periods $P^{\mathrm{I}} \geq 30$ s and $P^{\mathrm{II}} \approx 20$ s were observed. Of special interest is the spatial separation of the QPP sources with different periods. The region with the highest amplitude of pulsations with period $P^{\mathrm{I}} \geq 30$ s is localized in the inner part of the flaring loop, and QPPs with period $P^{\mathrm{II}} \approx 20$ s are localized at the periphery of the loop, near its footpoints. It is shown that the drift of the period found in the integrated (spatially unresolved) signal is a consequence of the gradual redistribution of radio brightness from the external part of the source to its internal part. Besides the spectral components with periods $P^{\mathrm{I}} \geq 30$ s and $P^{\mathrm{II}} \approx 20$ s, we also observed oscillations with period about $P^{\mathrm{III}} \approx 10$ s. Their spatial distribution is more complicated, containing three regions of high QPP amplitude: two near the footpoints and one in the middle of the flaring region. Another interesting result of our analysis is the observation of pairs of spectral components with close periods with a difference between them of about 13 % for both the component with $P \approx 30$ s and the component with $P \approx 20$ s. The presence of these components provides the effect of beating that is clearly seen in the wavelet spectra.

Comparison of spatial and spectral properties of the observed QPPs with results of a solution of the dispersion equation for MHD oscillations of a magnetic tube allowed us to choose the most appropriate MHD mode among potentially possible modes of standing MHD waves (acoustic, sausage, kink, and others). Based on strict limitations derived from data on the spatial structure of the pulsating flare region, we have shown that the observed

properties of the spectral components with periods $P^{\mathrm{I}} \approx 30$ s, $P^{\mathrm{II}} \approx 20$ s, and $P^{\mathrm{III}} \approx 10$ s are most accurately described by the fundamental, second, and third harmonics of the kink mode standing waves.

We believe that the observed microwave QPPs are produced by the gyrosynchrotron emission modulation caused by the kink mode standing waves. The distributions of the amplitudes and phases of the fundamental, second, and third harmonics of the kink mode along a magnetic loop provide spatial distributions rather similar to the observed distributions of the three main spectral components. Both horizontal and vertical kink modes are considered. An interesting property of the vertical kink mode is the oscillation of the magnetic field strength in the loop, similar to that in the sausage mode. Due to this effect, the vertical kink oscillations seem to provide a better explanation for the spectral component with period $P^{\mathrm{I}} \approx 30$ s than the horizontal oscillations. The maximum amplitude of this component is located in the middle part of the flaring loop. This observation can be easily explained by the vertical kink fundamental mode, which provides the strongest oscillations of the magnetic field strength in the upper part of the oscillating magnetic loop. We also provide some observational and theoretical evidence that kink mode oscillations of two adjacent thin loops can produce two spectral components with close periods, similar to the observed $\Delta P/P \approx 13\,\%$.

Kink mode oscillations in coronal magnetic loops were discovered more than a decade ago using TRACE EUV observations (Aschwanden *et al.*, 1999; Nakariakov *et al.*, 1999). Those loops were very large ($L \geq 100$ Mm), and the oscillations had large periods (minutes). On the other hand, solar flares provide oscillations in much smaller volumes and with much shorter time scales. Instruments like TRACE cannot resolve such oscillations because of their low temporal resolution; however, the NoRH microwave observations have sufficient spatial and temporal resolutions. To the best of our knowledge, the identification of the kink mode in a spatially resolved flaring loop was done in this study for the first time. Of special importance for this identification were spatial distributions of amplitudes and phases obtained for different spectral components. A further development of this method and its use for other flares opens new possibilities for studying QPP processes in solar flares.

Acknowledgements The *Nobeyama Radioheliograph* is operated by the Nobeyama Solar Radio Observatory/National Astronomical Observatory of Japan. This research was partly supported by grants of the Russian Foundation for Basic Research Nos. 11-02-91175 and 12-02-00616, the Program of the Russian Academy of Sciences No. 22, the Federal Program "Kadry" Nos. P683/20.05.2010 and 8524, "Scientific School" No. 1625.2012.2, and the Program MC FP7-PEOPLE-2011-IRSES-295272. V.M. is supported by the Chinese Academy of Sciences visiting professorship for senior international scientists with grant No. 2010t2j36. The authors express their special gratitude to V. Nakariakov for helpful discussions and to V. Grechnev for the codes for stabilization of the images and calculation of the variance map.

References

Andries, J., Arregui, I., Goossens, M.: 2005, *Astrophys. J. Lett.* **624**, L57.
Aschwanden, M.J., Fletcher, L., Schrijver, C.J., Alexander, D.: 1999, *Astrophys. J.* **520**, 880.
Aschwanden, M.J., Schrijver, C.J.: 2011, *Astrophys. J.* **736**, 102.
Diaz, A.J.: 2006, *Astron. Astrophys.* **456**, 737.
Dulk, G.A., Marsh, K.A.: 1982, *Astrophys. J.* **259**, 350.
Edwin, P.M., Roberts, B.: 1983, *Solar Phys.* **88**, 179.
Inglis, A.R., Nakariakov, V.M.: 2009, *Astron. Astrophys.* **493**, 259.
Kupriyanova, E.G., Melnikov, V.F., Nakariakov, V.M., Shibasaki, K.: 2010, *Solar Phys.* **267**, 329.
Melnikov, V.F., Reznikova, V.E., Shibasaki, K., Nakariakov, V.M.: 2005, *Astron. Astrophys.* **439**, 727.
Mészárosová, H., Karlický, M., Rybák, J., Fárník, F., Jiřička, K.: 2006, *Astron. Astrophys.* **460**, 865.
Mossessian, G., Fleishman, G.D.: 2012, *Astrophys. J.* **748**, 140.

Nakariakov, V.M., Ofman, L., DeLuca, E.E., Roberts, B., Davila, J.M.: 1999, *Science* **285**, 862.
Nakariakov, V.M., Melnikov, V.F.: 2009, *Space Sci. Rev.* **149**, 119.
Nakariakov, V.M., Melnikov, V.F., Reznikova, V.E.: 2003, *Astron. Astrophys.* **412**, L7.
Nakariakov, V.M., Verwichte, E.: 2005, *Living Rev. Solar Phys.* **3**, 1.
Stepanov, A.V., Kopylova, Y.G., Tsap, Y.T., Shibasaki, K., Melnikov, V.F., Goldvarg, T.B.: 2004, *Astron. Lett.* **30**, 480.
Stepanov, A.V., Zaitsev, V.V., Kisliakov, A.G., Urpo, S.: 2009, *Commun. Asteroseismol.* **159**, 30.
Tsap, Yu.T., Kopylova, Yu.G., Stepanov, A.V., Melnikov, V.F., Shibasaki, K.: 2008, *Solar Phys.* **253**, 161.
Van Doorsselaere, T., Ruderman, M.S., Robertson, D.: 2008, *Astron. Astrophys.* **485**, 849.
Verwichte, E., Foullon, C., Nakariakov, V.M.: 2006, *Astron. Astrophys.* **446**, 1139.
Wang, T.J., Solanki, S.K.: 2004, *Astron. Astrophys.* **421**, L33.
Zaitsev, V.V., Stepanov, A.V.: 1975, *Geomagn. Aeron. Fiz. Soln.* **37**, 3.
Zaitsev, V.V., Stepanov, A.V.: 2008, *Phys. Usp.* **51**, 1123.